PERGAMON

Available online at www.sciencedirect.com

SCIENCE DIRECT®

Continental Shelf Research 22 (2002) 2615–2631

CONTINENTAL SHELF RESEARCH

www.elsevier.com/locate/csr

Lateral dynamic analysis and classification of barotropic tidal inlets

James L. Hench[a,*], Brian O. Blanton[b], Richard A. Luettich Jr.[a]

[a] *Institute of Marine Sciences, University of North Carolina at Chapel Hill, 3431 Arendell Street, Morehead City, NC 28557, USA*
[b] *Department of Marine Sciences, University of North Carolina at Chapel Hill, 12-7 Venable Hall, CB 3300, Chapel Hill, NC 27599, USA*

Received 21 December 2000; accepted 6 March 2002

Abstract

The dynamical balances at shallow tidal inlets are highly nonlinear, and can vary substantially over sub-kilometer scales. In this study, barotropic dynamics are examined with numerical experiments on a series of idealized inlets with differing inlet widths and lengths. Circulation and elevation fields obtained from fully nonlinear depth-integrated circulation models are used to reconstruct the contribution of each term in the momentum equations. Momentum terms are rotated into a streamline coordinate system to simplify interpretation of the dynamics. Spatial patterns in momentum reveal that the lateral balances at inlets can vary from nearly geostrophic to strongly cyclostrophic. Marked dynamical differences are seen between inlets with different lengths and widths. Inlet regions of geostrophic or cyclostrophic balances can be predicted using two dimensionless parameters, the dynamic length L^* and dynamic width W^*. A classification scheme is proposed using L^* and W^* to compare the idealized inlets analyzed here with inlets from 20 previous studies. Four distinct inlet types are identified and discussed.

Keywords: Tidal inlet; Momentum balances; Streamline coordinates; Cyclostrophic; Geostrophic; Classification

1. Introduction

In the vicinity of an inlet with two opposing headland features, one might expect dynamical similarities to single headland flows (e.g. Signell and Geyer, 1991), and if this is the case, the dynamics are, at a minimum, two-dimensional. Since the dynamics are also highly nonlinear, analytical analysis is rather intractable for the most general cases. However, multidimensional numerical models are widely available, and amenable to momentum balance calculations as the physics included in the model are known a priori, and the circulation fields are deterministic. Several previous studies have used numerical coastal circulation models to study inlet dynamics. Imasato (1983) developed a set of force balance cartoons based on the results of an idealized inlet model. Ridderinkhof (1988) computed steady-state momentum balance values using a model of a natural inlet in the Wadden Sea. Imasato et al. (1994) computed vertical profiles of momentum at selected points for another idealized inlet. Hench and Luettich (in review) studied changes in

*Corresponding author. Tel.: +1-252-726-6841; fax: +1-252-726-2426.
E-mail address: hench@unc.edu (J.L. Hench).

0278-4343/02/$ - see front matter
PII: S0278-4343(02)00117-6

momentum balances over a tidal cycle for both a natural inlet and a complementary idealized inlet. These studies have provided valuable insight into fundamental circulation dynamics. However, given that each study has used different tidal forcing, inlet geometry, latitude, and bathymetry, two questions arise. First, how comparable are the results between the differing inlets, and second, how well do these intensive studies compare with other systems where the circulation is known to some degree, but the dynamics have not been thoroughly analyzed?

In this study we examine these questions with a set of numerical experiments on a series of idealized inlets (Section 2). In Sections 3 and 4, we use the velocity and elevation fields from the models to compute term by term momentum balances and Rossby numbers to identify the primary dynamical balances. The emphasis is on lateral dynamics, but we include the streamwise momentum balances as well to more fully understand cross-stream balances. Section 5 uses the insight gleaned from the momentum balance analyses to develop an inlet classification scheme where the results from this study are compared with those from 20 previous inlet studies. Finally, Section 6 provides discussion and conclusions.

2. Methods

2.1. Circulation modeling

We focus on barotropic dynamics and assume density gradients are dynamically small, as these conditions are common at shallow tidal inlets where vertical mixing is strong. These assumptions permit the use of the depth-integrated fully nonlinear barotropic shallow-water equations, which are solved using the circulation model ADCIRC (Luettich et al., 1992). Assuming no wind or tidal potential forcing, and a constant lateral viscosity, the governing continuity and momentum equations used in the model are

$$\frac{\partial \eta}{\partial t} + \frac{\partial UH}{\partial x} + \frac{\partial VH}{\partial y} = 0, \tag{1}$$

$$\frac{\partial U}{\partial t} + U\frac{\partial U}{\partial x} + V\frac{\partial U}{\partial y} - fV + g\frac{\partial \eta}{\partial x} - v\nabla^2 U + \left(\frac{C_f\sqrt{U^2+V^2}}{H}\right)U = 0, \tag{2}$$

$$\frac{\partial V}{\partial t} + U\frac{\partial V}{\partial x} + V\frac{\partial V}{\partial y} + fU + g\frac{\partial \eta}{\partial y} - v\nabla^2 V + \left(\frac{C_f\sqrt{U^2+V^2}}{H}\right)V = 0, \tag{3}$$

where x, y are horizontal coordinates aligned in East and North directions; $U(x, y, t)$, $V(x, y, t)$ are depth-integrated velocities; $H(x, y, t) = h(x, y) + \eta(x, y, t)$ is the total water column; $\eta(x, y, t)$ is the vertical displacement from the still water surface; $f(y)$ is the Coriolis parameter; g is gravity; v is the lateral eddy viscosity/dispersion coefficient; $\nabla^2 = \partial^2/\partial x^2 + \partial^2/\partial y^2$ is the horizontal diffusion operator; and C_f is the quadratic bottom friction coefficient. The model has been previously verified in studies of natural tidal inlets (see Luettich et al., 1999; Militello and Zarillo, 2000) and should faithfully simulate the physics of barotropic flow.

Four idealized inlet models (I–IV) were run, all identical except for inlet geometry (Fig. 1). The inlet geometries were selected to be representative of a range found in nature. The computational domains consisted of two rectangular basins, representing an ocean shelf and a sound (also known as a bay or lagoon), and connected by a single inlet. Basin dimensions were the same in each of the models to isolate the effects of inlet geometry. The bathymetry for each of the models was also the same, with water depths in the sounds and inlets uniformly 5 m, while offshore the depths increased linearly from 5 to 14 m at the open boundaries. Grid resolution ranged from 1 km at the open boundaries to a uniform 50 m in the vicinity of the inlets. All four models were forced along an offshore ocean boundary with specified elevations of 0.15 m amplitude and zero phase at the M_2 frequency. This forcing was selected to produce maximum velocities in the inlet throat of about $1\,m\,s^{-1}$ for the two "narrow" inlets (I and II). The remaining boundaries were treated as land, with zero normal velocity boundary conditions. For all model runs, a constant Coriolis

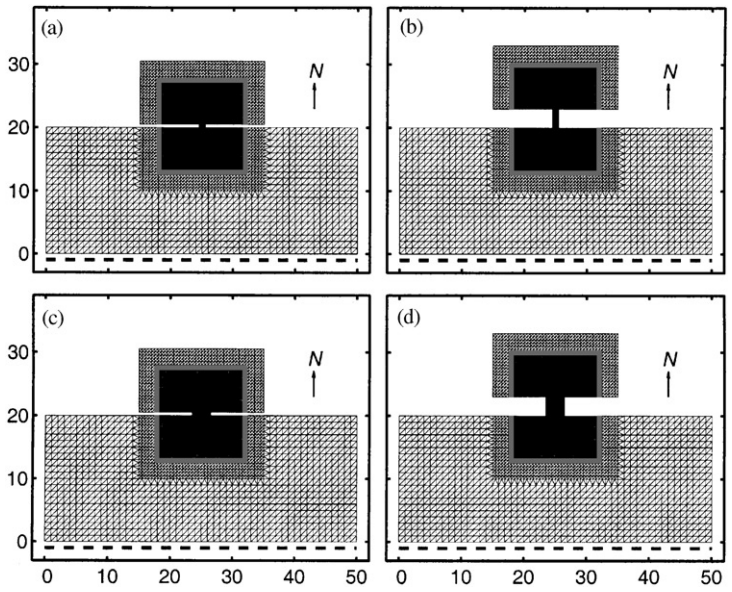

Fig. 1. Computational grids used in momentum balance analyses. (a) idealized inlet I (0.5×1.0 km), (b) idealized inlet II (3.0×1.0 km), (c) idealized inlet III (0.5×3.0 km), (d) idealized inlet IV (3.0×3.0 km), where inlet dimensions are given in parentheses. Thick dashed lines indicate locations of open boundary forcing. The other boundaries are treated as land, with zero normal flow boundary conditions applied. Axes distances are given in kilometers.

parameter was used corresponding to latitude 34.5 degrees N. The lateral viscosity was set to a constant value of $4\,m^2\,s^{-1}$, and a constant bottom friction coefficient of 0.0025 was used. The models were spun-up from rest and run for 4 days to dynamic equilibrium using a time-step of 4 s.

2.2. Momentum balance calculations

Velocity and elevation fields from the models were used to evaluate each term in the $x-y$ momentum Eqs. (2) and (3) at every computational node. Each term was evaluated using exactly the same integration, assembly scheme, and run parameters as in the circulation model (see Luettich et al., 1992 for details) so that the individual momentum terms were consistent with the computed flow fields. For visualization and interpretation purposes, a rotational transform was applied to the precomputed $x-y$ components of each term in the momentum equations, which yielded the corresponding momentum term values in a streamwise-normal ($s-n$) coordinate system. Appendix A details the coordinate rotation and transform (see Eqs. (A.1)–(A.4)). Momentum was conserved at all grid points in both the x and y directions, as well as the s and n directions, typically to within one percent of the largest term in the local momentum balance. Conservation was not perfect due to the finite precision arithmetic in the numerical integration of the momentum terms, but the errors were small enough not to affect interpretation of the momentum balances. Rotated momentum fields were interpreted using the $s-n$ momentum equations (also derived in Appendix A)

$$\underbrace{\frac{\partial U_s}{\partial t}}_{\substack{\text{local}\\ \text{streamwise}\\ \text{acceleration}}} \underbrace{+U_s\frac{\partial U_s}{\partial s}}_{\substack{\text{streamwise}\\ \text{(Bernoulli)}\\ \text{acceleration}}} \underbrace{+g\frac{\partial \eta}{\partial s}}_{\substack{\text{streamwise}\\ \text{pressure}\\ \text{gradient}}} \underbrace{+\frac{C_f U_s^2}{H}}_{\substack{\text{nonlinear}\\ \text{bottom}\\ \text{friction}}} = 0, \tag{4}$$

$$\underbrace{U_s\frac{\partial \alpha}{\partial t}}_{\substack{\text{local}\\ \text{rotary}\\ \text{acceleration}}} \underbrace{+\frac{U_s^2}{R_s}}_{\substack{\text{centrifugal}\\ \text{acceleration}}} \underbrace{+fU_s}_{\substack{\text{Coriolis}\\ \text{acceleration}}} \underbrace{+g\frac{\partial \eta}{\partial n}}_{\substack{\text{normal}\\ \text{direction}\\ \text{pressure}\\ \text{gradient}}} = 0, \tag{5}$$

where $U_s(x, y, t)$ is the streamwise velocity, $R_s(x, y, t)$ is the flow radius of curvature, and

$\alpha(x, y, t)$ is the streamline angle (the angle between the positive x-axis and the local flow vector). With this choice of coordinate system there is, by definition, no normal component to the flow at any point. Therefore the Coriolis term is zero in the s-equation, as is the bottom friction term in the n-equation. Moreover, the advective acceleration terms collapse to a single term in each equation; streamwise in the s-equation and centrifugal in the n-equation. The horizontal diffusion/dispersion terms were generally much smaller than the other terms, and are omitted from Eqs. (4) and (5), as well as the discussion below. Results are presented in terms of momentum fluxes (obtained by multiplying each term by the total water column) to provide a more physically intuitive picture of the force balances.

3. Momentum balances

Although inlet momentum balances change dramatically over a tidal cycle, previous results (Hench and Luettich, in review) have shown that the dominant balances for the majority of the time are quite similar to what is found during maximum flood and maximum ebb. Here we focus on a single tidal phase, maximum flood, to explore the effects of different inlet configurations. Maximum flood was defined as the time of maximum velocity at a point located at the geometric center of the southern end of each inlet. Momentum balances are shown for each inlet in Figs. 2–5.

3.1. Idealized inlet I

Circulation and momentum balances for idealized inlet I are shown in Fig. 2. The flow is strongest within the inlet straits and symmetric transient eddies are seen on the sound side of the inlet (Fig. 2a). The flow has reached near steady state in both the streamwise and normal directions as evident by small local accelerations, except within the center of the transient eddies (Figs. 2d and h). The primary streamwise momentum balances occur in two distinct zones. On the ocean side (the "sink" region), the main balance is between the streamwise pressure gradient and the streamwise acceleration (Figs. 2e and f). However on the sound side of the inlet (the "jet" region), the flow is decelerating (Fig. 2e) under the influence of bottom friction (Fig. 2g). In the normal direction, the rotary acceleration (Fig. 2h) is small except in the center of the transient eddies (Fig. 2a). The primary lateral balance within the entire inlet straits is between the centrifugal acceleration and the normal direction pressure gradient (Figs. 2i and j). Coriolis is strongest within the inlet straits where the flow speeds are largest (Fig. 2k), but is overwhelmed by the centrifugal acceleration.

3.2. Idealized inlet II

Inlet II has the same width as inlet I but is 2.5 km longer. The local accelerations are small (Figs. 3d and h). In the streamwise direction, there are two distinct momentum balance zones, but they are different than for inlet I. Immediately offshore from the inlet the primary balance is between the streamwise pressure gradient and the streamwise acceleration (Figs. 3e and f). In the inlet straits, however, the balance is between the pressure gradient and bottom friction (Figs. 3f and g). There are two small flow separation areas in the lee of the inlet headlands where adverse pressure gradients (Fig. 3f) are balanced by streamwise deceleration (Fig. 3e). The normal direction balances exhibit two zones as well. Near the inlet mouth centrifugal acceleration and lateral pressure gradients dominate (Figs. 3i and j). But within the straits, the balance is between Coriolis and the normal direction pressure gradient (Figs. 3j and k). On the sound side of the inlet (not shown in Fig. 3) the balances in both the streamwise and normal directions resemble those seen on the sound side of inlet I. The balances for this inlet are distinct from inlet I in that a middle zone appears where advective accelerations (i.e. streamwise and centrifugal) tend toward zero. Here the streamlines are straight and the flow radius of curvature approaches infinity.

3.3. Idealized inlet III

Inlet III has the same length as inlet I, but the headlands were spaced 2 km wider. The flows

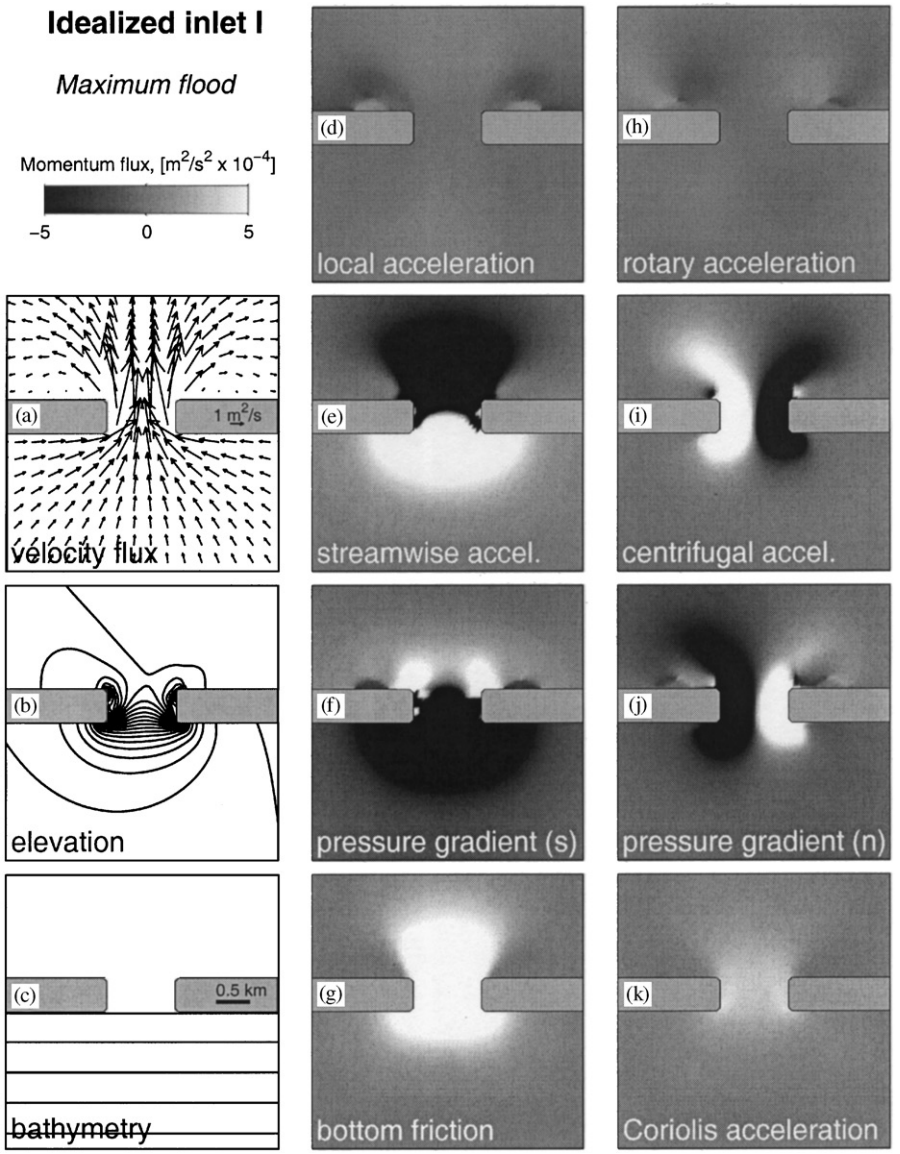

Fig. 2. Circulation and momentum balances for idealized inlet I at maximum flood: (a) velocity flux, the depth-averaged velocity multiplied by total water column (velocity vectors have been interpolated to a coarser grid with 250 m spacing for clarity); (b) free surface elevation with 0.5 cm contour intervals; (c) bathymetry with 0.2 m contour intervals; (d–k) shaded contours of individual momentum flux terms (see text for description). The middle column of subplots contains the streamwise momentum terms, the rightmost column contains normal direction momentum terms.

adjacent to the headlands are much stronger than in the center of the inlet (Fig. 4a). The transient eddies that were so pronounced in the sound for inlet I are not present here, and the corresponding local acceleration terms in this area are small (Figs. 4d and h). Near the headlands, streamwise direction balances are primarily between the streamwise acceleration and pressure gradient (Figs. 4e and f). Bottom friction is important near the headlands as well (Fig. 4g); the spatial pattern

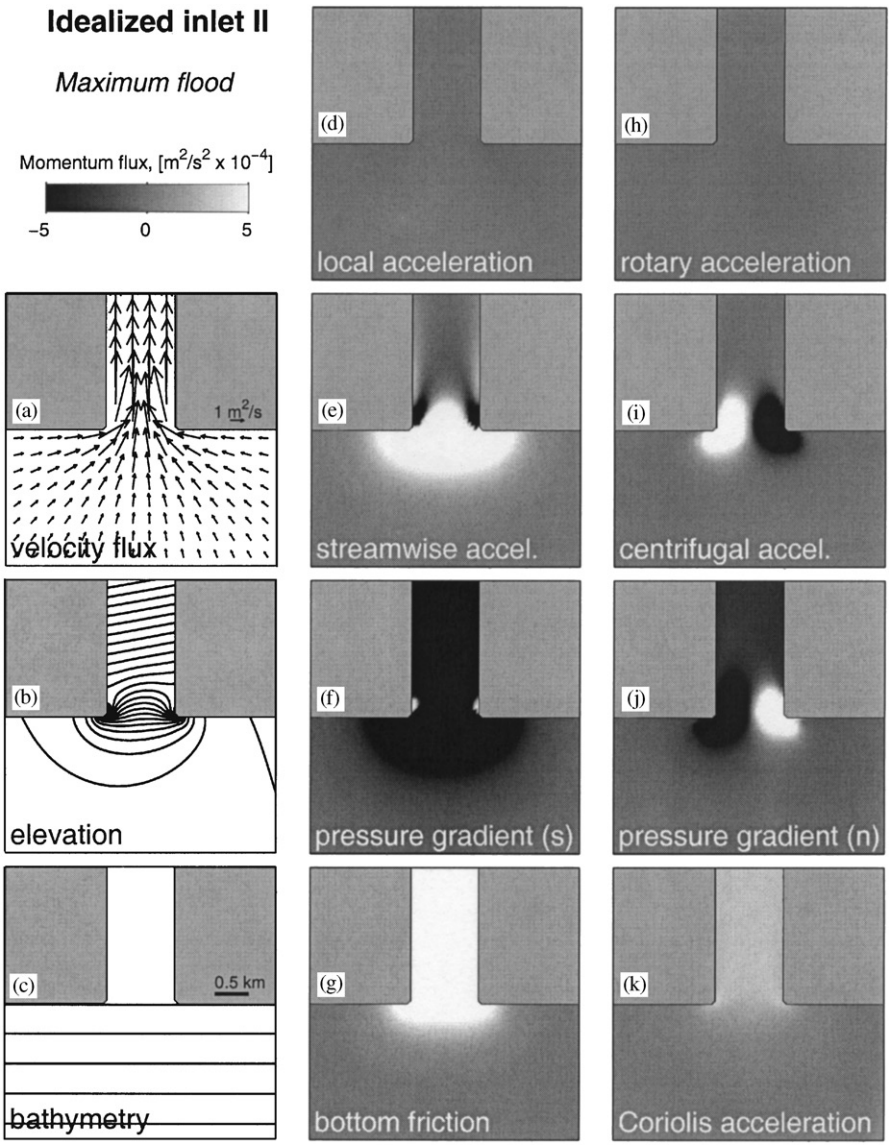

Fig. 3. Circulation and momentum balances for idealized inlet II, otherwise same as Fig. 2.

is similar to the flow field since in the rotated coordinate system the streamwise velocity is equivalent to the flow speed. In the normal direction centrifugal accelerations balance the lateral pressure gradients along the entire inlet length, but are confined to regions adjacent to the headlands (Figs. 4i and j). Along the center region of this inlet, it is not immediately obvious from Fig. 4 whether centrifugal or Coriolis accelerations dominate; we will examine this point in more detail in Section 4.

3.4. Idealized inlet IV

Fig. 5 shows the momentum balances for inlet IV. Here the dynamics are a combination of those found for inlets II and III. Flood flow is driven by a strong favorable (negative) pressure

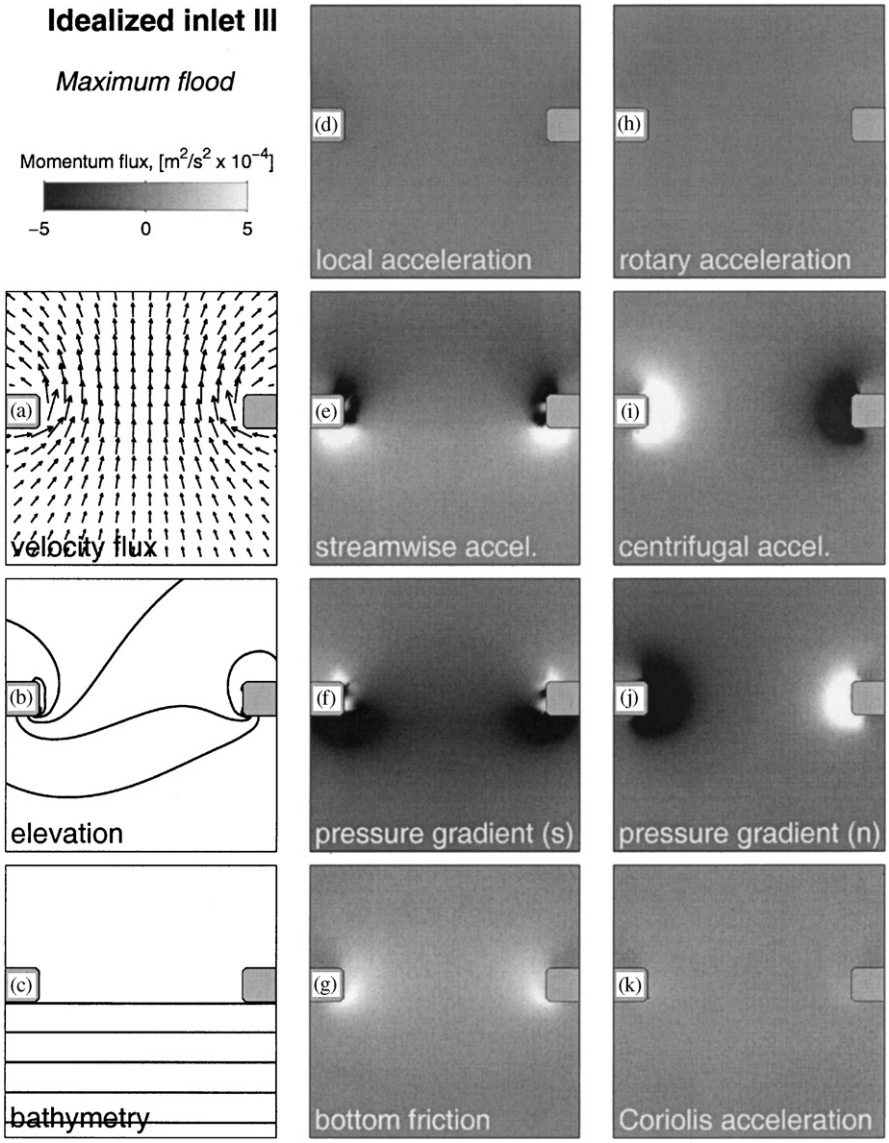

Fig. 4. Circulation and momentum balances for idealized inlet III, otherwise same as Fig. 2.

gradient (Fig. 5f). Near the inlet headlands there is strong streamwise acceleration as the flow enters the inlet, but strong deceleration in the immediate lee of the headlands (Fig. 5e). The areas of positive pressure gradient in the lee of the headlands are associated with flow separation. Further into the inlet straits, the streamwise balance along and across the inlet reverts to one between pressure gradient and bottom friction (Figs. 5f and g). The normal direction balances also show strong spatial variability. The centrifugal acceleration versus lateral pressure gradient momentum balances are clearly dominant near the headlands (Figs. 5i and j). The pattern is similar at the other end of the inlet (not shown). In the center of the inlet, and within the inlet straits is a region of pressure gradient balanced by Coriolis acceleration.

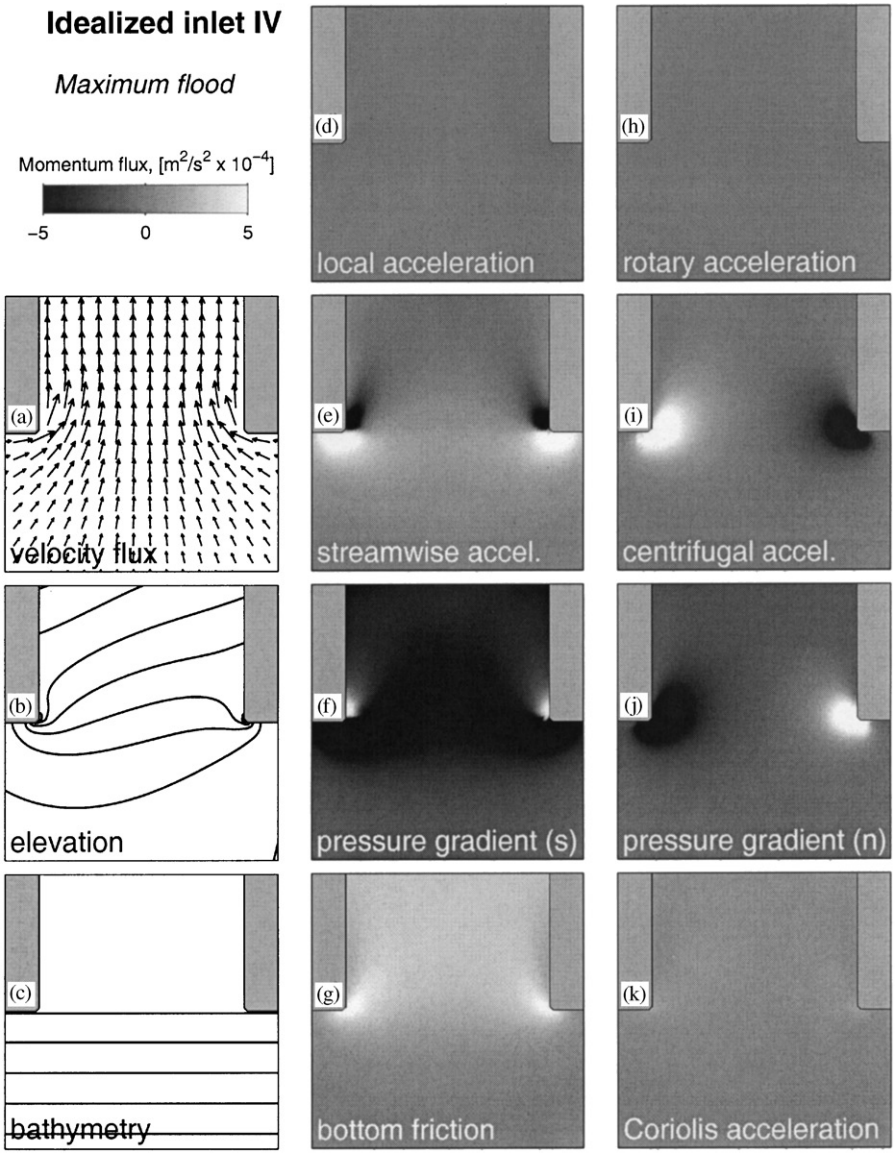

Fig. 5. Circulation and momentum balances for idealized inlet IV, otherwise same as Fig. 2.

3.5. Model sensitivity

A series of additional model runs were made to test sensitivity to model parameters. Runs with the bottom friction coefficient C_f set to 0.0020 and 0.0030 were compared against the baseline run with $C_f = 0.0025$. Results showed the decreased C_f generally increased the magnitude of near inlet streamwise momentum fields typically by 10%. Increased C_f had the reverse effect. The cross-stream momentum balances were indirectly affected, since bottom friction does not appear in the rotated n-equation. Reducing C_f increased flow speeds yielding larger centrifugal accelerations and steeper normal direction pressure gradients. However, overall patterns in all momentum terms were only modestly changed within this range of C_f values. Model sensitivity to viscosity was tested

with runs where ν was set to $2\,m^2\,s^{-1}$, $4\,m^2\,s^{-1}$ (the baseline), and $6\,m^2\,s^{-1}$. The $2\,m^2\,s^{-1}$ run showed sharper velocity gradients, but was contaminated by high frequency numerical oscillations in the momentum fields, while the $6\,m^2\,s^{-1}$ run exhibited comparatively smooth velocity gradients and momentum fields. In all three runs the major features of the momentum balances were unchanged. The model was most sensitive to changes in depth. Runs where the sound and inlet bathymetry were set shallower (3 m) and deeper (7 m) were compared with the baseline run with 5 m depth. Results were as expected, with the shallower depth producing stronger streamwise accelerations and bottom friction (both balanced by a steeper streamwise pressure gradient). Spatial structure of the lateral balance was unchanged, but with stronger centrifugal accelerations and lateral pressure gradients. Increasing the depth had the opposite effects, but again did not change the major momentum features.

4. Lateral dynamics and Rossby numbers

The results of our analysis on the four idealized inlets indicate that at the stronger phases of the tide, the flow is near steady state and lateral diffusion of momentum is small. Therefore the lateral momentum balance reduces to the sum of centrifugal and Coriolis accelerations and the lateral pressure gradient

$$\frac{U_s^2}{R_s} + fU_s + g\,\frac{\partial \eta}{\partial n} = 0. \tag{6}$$

We now look at the two limiting cases. If centrifugal acceleration is negligible then (Eq. 6) reduces to a geostrophic balance

$$fU_s + g\,\frac{\partial \eta}{\partial n} = 0, \tag{7}$$

and conversely, if the centrifugal acceleration is much greater than Coriolis (Eq. 6) can be approximated by a cyclostrophic balance

$$\frac{U_s^2}{R_s} + g\,\frac{\partial \eta}{\partial n} = 0. \tag{8}$$

We now assess the relative importance of the centrifugal and Coriolis accelerations. In the context of the rotated coordinate system we form a "curvature" Rossby number

$$R_0 = \left|\frac{\dfrac{U_s^2}{R_s}}{fU_s}\right| = |U_s/fR_s|. \tag{9}$$

Model results were used to directly compute R_0 throughout the flow, as shown in Fig. 6 for each of the idealized inlets. For inlet I, $R_0 > 1$ over the entire width and length of the inlet (Fig. 6a). There is a marked asymmetry between the ocean side and the sound side of the inlet. The region of high R_0 on the sound side is enhanced by the centrifugal acceleration of the transient tidal eddies. For inlet II (Fig. 6b), the high R_0 region still spans the entire inlet width, but the centrifugal acceleration and R_0 sharply diminish within the straits. For inlet III (Fig. 6c), R_0 is large in regions adjacent to the inlet headlands and along the entire inlet length, but there is a region of low R_0 in the inlet center. Finally, inlet IV exhibits R_0 patterns that are a combination of inlets II and III (Fig. 6d), with high R_0 only near the inlet headlands. By convention R_0 is always positive but we note that it reaches zero in the middle of each of the inlets at the location where the radius of curvature becomes infinite. At these locations the radius of curvature changes sign from positive (on the west sides) to negative (on the east sides). Results from a companion study of transient dynamics (Hench and Luettich, in review) showed that these balances hold for much of the tidal cycle but not during the weaker phases, particularly during the hour nearest to slack. During those tidal phases, $R_0 \ll 1$ but the balances are still not geostrophic as the local acceleration terms are important.

5. Inlet classification scheme

Our analysis of inlet dynamics has identified the dominant force balances for a range of inlet configurations. In this section, we use this insight to develop an inlet classification scheme based on these underlying dynamics. Previous classification schemes have been developed for estuarine circulation (Stommel and Farmer, 1952; Hansen and

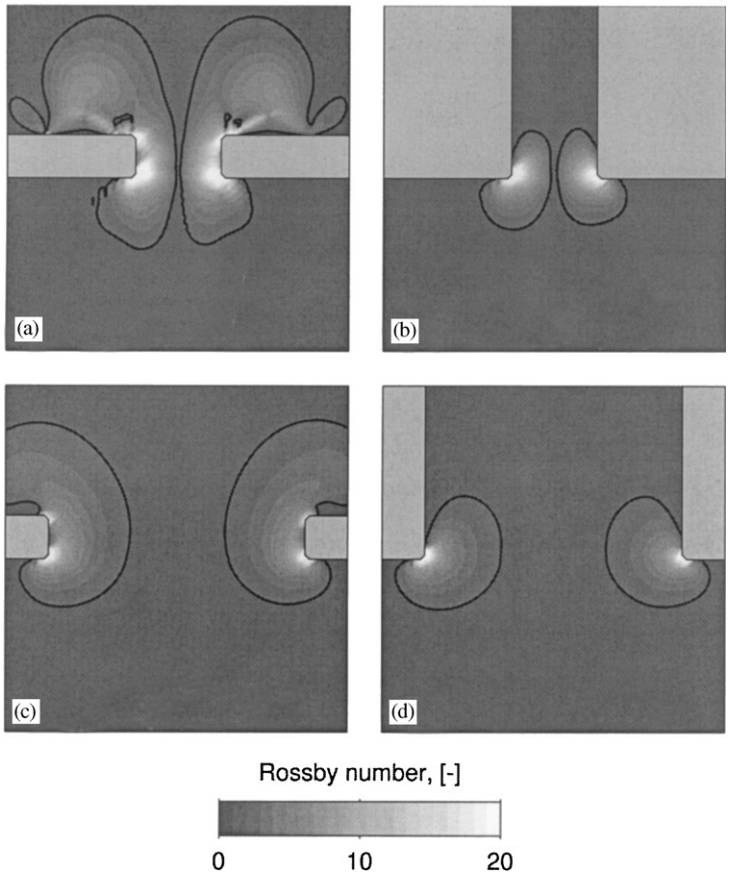

Fig. 6. Computed Rossby number (defined as $R_0 = |U_s/fR_s|$) shaded contours for the four idealized inlets at maximum flood. The solid black contour lines indicate $R_0 = 1$.

Rattray, 1966; Jay and Smith, 1988) as well as for buoyant coastal discharges (Garvine, 1995; Kourafalou et al., 1996). Thoughtful reviews of classification schemes are given by Dyer (1997) and by Jay et al. (2000). Much less work has been done for inlet classification, although inlets have been classified following the Hayes (1979) barrier island scheme. The Hayes classification uses mean wave height and mean tidal range to assess the relative role these two processes play in shaping barrier island morphology. The scheme has subsequently been used for inlet classification, but the physical justification for this seems limited. One can imagine two inlets in close proximity along a coast with similar mean tidal ranges and mean wave heights. These two inlets would be classified the same using Hayes (1979). However, if the inlets' tidal prism and inlet geometry were dissimilar, they may have very different tidal circulation and dynamics. Thus the lack of any inlet geometry or velocity characteristics appears to be a significant weakness in extending the Hayes (1979) scheme to tidal inlets.

Here we develop a new inlet classification scheme based on two dimensionless parameters derived from the lateral tidal momentum balances and intrinsic inlet geometry. Following the results from Section 4, we first find the length scale at which the centrifugal and Coriolis accelerations are comparable. Setting $R_0 = 1$ and solving for R_{s1}, the radius of curvature for which the Rossby number is one

$$R_{s1} = U_s/f. \tag{10}$$

R_{s1} is the length scale at which the centrifugal and Coriolis accelerations come into balance (also known as the inertial radius). We now want to compare R_{s1}, the length scale set by the dynamics, with the inlet geometric length scales. We define the dynamic length and dynamic width as

$$L^* = \frac{(L/2)}{R_{s1}} \quad W^* = \frac{(W/2)}{R_{s1}}, \tag{11}$$

where the inlet length and width scales, L and W, are divided by two because of symmetry. The physical interpretations of L^* and W^* are straightforward. First consider flow curving around headlands at a very wide inlet (or taken to the limit, around a single headland, i.e. $W = \infty$). Adjacent to either of the headlands one would expect the momentum balance to be cyclostrophic. However, with increasing distance from a headland the centrifugal acceleration diminishes, and the water surface relaxes into a cross-stream balance with Coriolis. Here the inlet width does not constrain the lateral dynamics, and W^* is large. Thus if the inlet is much wider than the inertial radius, flow around each headland is not in strong dynamic communication with the opposing headland. Now consider a narrower inlet. The balance at each of the opposing headlands is still cyclostrophic, but here the inlet width is too narrow for the water surface in the middle of the inlet to relax to geostrophy. Rather, the centrifugal acceleration from each headland is balanced by opposing pressure gradients, forming a "dome" of water across the inlet. Since the barotropic pressure gradient is uniform with depth, flow around each headland is effectively constrained to one side of the inlet, in much the same way as the solid outside boundary pushes against the flow around a river bend. In this case W^* is small and the flows around each headland are in strong dynamic communication. A similar dynamical situation exists along the length of the channel. When the inertial radius is greater than the geometric length (small L^*) then the balance is cyclostrophic along the entire length of the inlet. Conversely, a large L^* would indicate that a geostrophic region exists within the inlet straits.

We use these two parameters to classify and compare inlets from previous studies. Parameters for 20 inlets were taken from the literature and combined with those for the four inlets analyzed in this study (see list in Fig. 7). The inlets chosen are not an exhaustive list, but should be representative of many inlets found in nature. The velocity scales were chosen from published values for maximum ebb or flood. In some cases, parameter values were estimated from published figures when the actual numbers were not cited, so the values used here may not be exact.

The inlet classification diagram using L^* versus W^* is shown in Fig. 7. For the 24 inlets analyzed the parameter space for both L^* and W^* spans over an order of magnitude. Since f varies only by a factor of 3 among the inlets, most of the variance in L^* and W^* is due to differences in flow speed (varies by a factor of 10) and geometry (L varies by a factor of 15, W by a factor of 80). The clustering of data around a line $L^* = W^*$ suggests that in nature there is a tendency for the aspect ratio of dynamic lengths to widths to be close to one. The correlation between L^* and W^* may be a consequence of flow having feedback with a movable seabed and tending toward equilibrium topography. However many of these inlets are fictitious (idealized) and others have been modified by jetties and dredging. We tentatively picked 0.1 as the dividing line between "narrow" and "wide", and between "short" and "long"; based on the results of our numerical experiments, this appears to be roughly where the transition takes place. These lines should provide a rough guide of which dynamical regime one might expect an inlet to fall within.

6. Discussion and conclusions

Our analysis of inlet dynamics has shown that momentum balances can vary significantly over sub-kilometer scales. Near the inlet headlands, and often over the entire inlet, the first-order balances are the pressure gradient and a combination of different nonlinear terms. A common assumption in one-dimensional inlet analyses is that the streamwise pressure gradient is balanced by nonlinear bottom friction. Our two-dimensional results indicate this assumption is only valid within

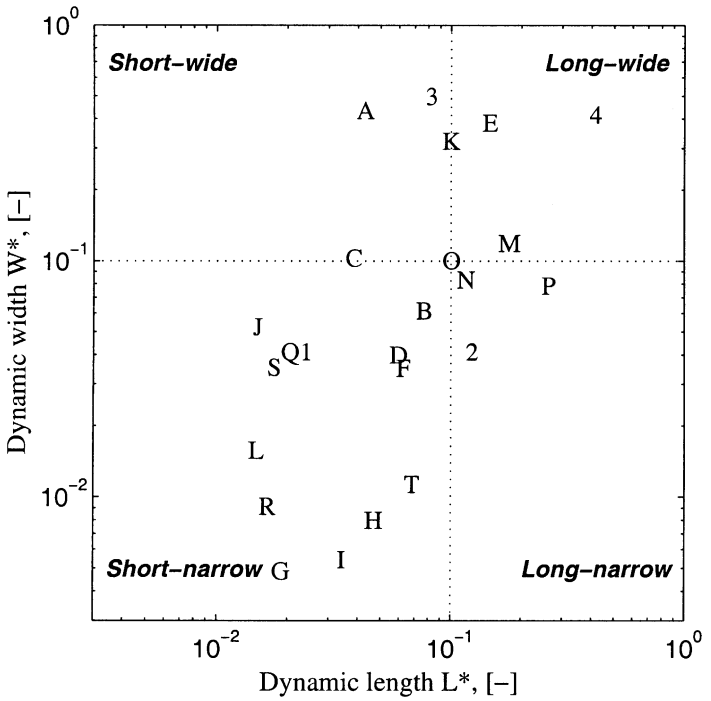

Fig. 7. Inlet classification diagram based on barotropic lateral dynamics. Parameter values for 20 inlets from the literature are plotted with the 4 inlets analyzed in this paper.

ID	Inlet description	References
A	Sandy Hook-Rockaway Pt., New York	Doyle and Wilson (1978)
B	Idealized inlet	Awaji et al. (1980)
C	Idealized inlet	Imasato (1983)
D	The Cut, Koombana Bay, Australia	Hearn et al. (1985)
E	Zeegat van het Vlie, Netherlands	Ridderinkhof (1988)
F	Ribbon Reefs 3 and 4, Australia	Wolanski et al. (1988)
G	Indian River Inlet, Delaware	Wong and DiLorenzo (1988)
H	Wells Inlet, Maine	Mariano and FitzGerald (1991)
I	Sebastian Inlet, Florida	Liu (1992)
J	Port Phillip Bay, Australia	Black et al. (1993)
K	Idealized inlet	Imasato et al. (1994)
L	Essex River Inlet, Massachusetts	Smith and FitzGerald (1994)
M	Idealized inlet	Kapolnai et al. (1996)
N	Idealized inlet	Wheless and Valle-Levinson (1996)
O	Puerto Real Inlet, Mexico	David and Kjerfve (1998)
P	San Diego Bay, California	Chadwick and Largier (1999)
Q	Beaufort Inlet, North Carolina	Luettich et al. (1999)
R	Shinnecock Inlet, New York	Militello et al. (2000)
S	Ponce de Leon Inlet, Florida	Militello and Zarillo (2000)
T	Aransas Pass, Texas	Brown et al. (2000)
1	Idealized inlet I	This study
2	Idealized inlet II	This study
3	Idealized inlet III	This study
4	Idealized inlet IV	This study

the straits of dynamically long inlets or within the center region of dynamically wide inlets. For dynamically short inlets, and near the ends of dynamically long inlets, the streamwise and centrifugal accelerations are part of the first-order dynamics and need to be retained.

Our analysis of lateral momentum balances and comparison of natural inlet parameter values has shown a range of different dynamics that can occur. We have proposed a two parameter classification scheme for tidal inlets and identified four distinct inlet types:

Type 1. Dynamically short-narrow inlet (small L^* and small W^*), where a cyclostrophic lateral balance dominates the entire inlet straits.

Type 2. Dynamically long-narrow inlet (large L^* and small W^*), where at both ends of the inlet a cyclostrophic lateral balance dominates across the entire width, but relaxes to a geostrophic balance within the inlet straits.

Type 3. Dynamically short-wide inlet (small L^* and large W^*), where a cyclostrophic lateral balance dominates close to the headlands and extends along the entire length of the inlet. However, there is a center region along the entire inlet length where the lateral balance is geostrophic.

Type 4. Dynamically long-wide inlet (large L^* and large W^*), where a cyclostrophic lateral balance dominates only immediately adjacent to the four inlet headland corners, and a geostrophic balance exists everywhere else.

The idealized inlets analyzed here (I–IV) are archetypal examples for the classification. Estuarine systems are highly spatially variable, and thus multiple classification schemes may be needed for different regions (Jay et al., 2000). Our proposed classification scheme is applicable to the inlet straits and the region in the immediate vicinity of inlet headlands. The scheme fits spatially between previous estuarine classifications (more appropriate upstream of an inlet) and buoyant plume classifications (more appropriate offshore of an inlet). W^* in our scheme is similar in spirit to the mouth Kelvin number (ratio of baroclinic radius of deformation to river mouth width) of Garvine (1987), but the underlying dynamics are different. Garvine's work centered on sub-tidal propagation of buoyant plumes, and therefore neglected the barotropic tidal dynamics described here.

The classification diagram (Fig. 7) should be useful in comparing the relative dynamics of different inlet systems. However, as with all classification schemes, there are a number of limitations. The morphology at some natural inlets may be so convoluted that assigning representative lengths and widths may be difficult. Other inlets may have geometries so laterally asymmetric that they behave more like a river-bend than the opposing headland conceptual model described here. Inlets with river mouth morphologies do not fit well on the diagram since their dynamic lengths are so long, but would be classified as either type 2 or 4. Inlet morphology may change over time due to natural erosion and deposition, or anthropogenic activities such as dredging. It is conceivable that such morphological changes could significantly modify circulation patterns and dynamical balances to the extent that the inlet classification could shift or even change altogether.

For simplicity we have only examined tidal forcing and simple inlet geometries but real inlet circulation may have significant additional effects from: radiation stress and Stokes drift from wind waves, direct and remote wind forcing, phase differences in offshore tidal forcing, baroclinicity, steep bottom topography and irregular shoreline geometry. Circulation changes over a spring-neap cycle may also affect inlet classification as Jay and Smith (1988) showed in their estuarine classification scheme. We have conducted additional model runs (not shown) with increased forcing amplitudes and found that the two geometrically wide inlets in this study (III and IV) can change from dynamically wide to dynamically narrow inlets with sufficient forcing and accompanying increase in U_s.

Despite the simplifications the present analysis provides a rational framework with which to compare different inlet systems, and to put new studies in the context of previous work. For a classification scheme to be useful, it should be constructed in terms of readily observable parameters, yet it must still retain the essential physics. The proposed scheme succeeds in this regard, and to our knowledge is the first classification scheme

for inlets based on a dynamical analysis. The four idealized inlets analyzed here provide baseline cases for the dynamics one might expect at natural inlets.

Acknowledgements

We thank two anonymous reviewers for constructive comments that significantly improved the manuscript. Funding for this study was provided by the Coastal Inlets Research Program (CIRP) of the Coastal Hydraulics Laboratory, US Army Corps of Engineers, and the Naval Research Laboratory, Office of Naval Research (award N00014-97-C-6010).

Appendix A. Rotation of momentum equations into a streamwise-normal coordinate system

The use of a streamwise-normal coordinate system allows a more intuitive physical interpretation for strongly curving flow fields. Gill (1982) elegantly derives the steady frictionless form of the two-dimensional momentum equations directly in the $s-n$ coordinate system. Here we derive corresponding transient frictional equations by transforming the familiar $x-y$ equations. This transformation is useful in that standard $x-y$ momentum terms can be used to directly compute term values in the $s-n$ coordinate system. The procedure is as follows. $U(x,y,t)$, $V(x,y,t)$ and $\eta(x,y,t)$ are computed on a fixed $x-y$ grid for all time steps. The elevation and velocity fields are used to reconstruct each term in the $x-y$ momentum equations at each node in the $x-y$ grid. We designate the individual $x-y$ momentum terms M_{xi} and M_{yi} as

$$\underbrace{\frac{\partial U}{\partial t}}_{M_{x1}}\underbrace{+U\frac{\partial U}{\partial x}+V\frac{\partial U}{\partial y}}_{M_{x2}}\underbrace{-fV}_{M_{x3}}\underbrace{+g\frac{\partial \eta}{\partial x}}_{M_{x4}}\underbrace{+\left(\frac{C_f\sqrt{U^2+V^2}}{H}\right)U}_{M_{x5}}=0, \tag{A.1}$$

$$\underbrace{\frac{\partial V}{\partial t}}_{M_{y1}}\underbrace{+U\frac{\partial V}{\partial x}+V\frac{\partial V}{\partial y}}_{M_{y2}}\underbrace{+fU}_{M_{y3}}\underbrace{+g\frac{\partial \eta}{\partial y}}_{M_{y4}}\underbrace{+\left(\frac{C_f\sqrt{U^2+V^2}}{H}\right)V}_{M_{y5}}=0. \tag{A.2}$$

For simplicity, horizontal diffusion terms are omitted from (A.1) and (A.2) as they did not contribute significantly to the momentum balances of our inlet simulations. At each time-step, we define a two-dimensional, orthogonal, curvilinear coordinate system such that at each grid point, one coordinate direction points in the along-stream direction (s) and the other points in the across-stream direction (n) in the right hand sense (see Fig. 8). The orientation of the $s-n$ coordinate system relative to the original fixed $x-y$ coordinate system, as expressed by the streamline angle $\alpha(x,y,t)$, varies such that at all points the along-stream velocity U_s is equivalent to the speed, and the across-stream velocity $U_n = 0$. From Fig. 8, it should be apparent that momentum terms in $s-n$

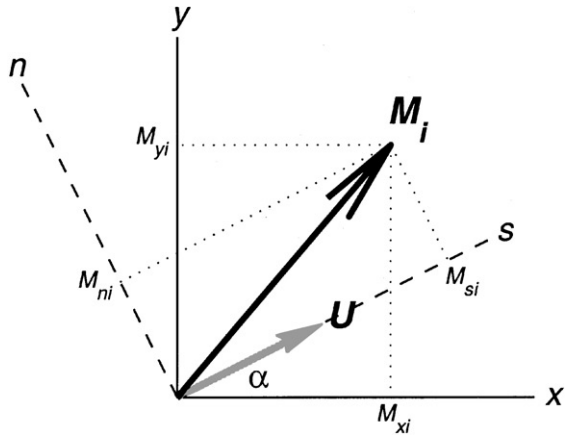

Fig. 8. Definition sketch for the streamline coordinate system. At each computational node a $s-n$ coordinate system is established and aligned with the local velocity vector U. The local axes rotation angle is $\alpha(x,y,t)$. M_i represents the ith force or acceleration vector in the momentum equations, with $x-y$ components M_{xi} and M_{yi} (e.g. $g\,\partial\eta/\partial x$ and $g\,\partial\eta/\partial y$). M_i is rotated on to the $s-n$ axes to determine local streamwise and normal components M_{si} and M_{ni} (e.g. $g\,\partial\eta/\partial s$ and $g\,\partial\eta/\partial n$).

coordinates are related to those in the $x-y$ coordinate system by

$$M_{si} = M_{xi}\cos\alpha + M_{yi}\sin\alpha, \tag{A.3}$$

$$M_{ni} = M_{yi}\cos\alpha - M_{xi}\sin\alpha, \tag{A.4}$$

where the index $i = 1:5$ as in Eqs. (A.1) and (A.2) above. The along- and across-stream velocities can be related to the $x-y$ velocity components using the same orthogonal rotation

$$U_s = U\cos\alpha + V\sin\alpha = \sqrt{U^2+V^2}, \tag{A.5}$$

$$U_n = V\cos\alpha - U\sin\alpha \equiv 0. \tag{A.6}$$

From Eq. (A.6), $\alpha = \arctan(V/U)$. Eqs. (A.5) and (A.6) can also be rearranged to express (U, V) in terms of U_s and α

$$U = U_s\cos\alpha, \tag{A.7}$$

$$V = U_s\sin\alpha. \tag{A.8}$$

Substituting the $x-y$ momentum terms from Eqs. (A.1) and (A.2) into Eqs. (A.3) and (A.4), and replacing U and V using Eqs. (A.7) and (A.8) gives

$$\underbrace{\frac{\partial U_s}{\partial t}}_{M_{s1}} \underbrace{+U_s\left(\cos\alpha\frac{\partial U_s}{\partial x} + \sin\alpha\frac{\partial U_s}{\partial y}\right)}_{M_{s2}} \underbrace{+g\left(\cos\alpha\frac{\partial\eta}{\partial x} + \sin\alpha\frac{\partial\eta}{\partial y}\right)}_{M_{s4}} \underbrace{+\frac{C_f U_s^2}{H}}_{M_{s5}} = 0, \tag{A.9}$$

$$\underbrace{U_s\frac{\partial\alpha}{\partial t}}_{M_{n1}} \underbrace{+U_s^2\left(\cos\alpha\frac{\partial\alpha}{\partial x} + \sin\alpha\frac{\partial\alpha}{\partial y}\right)}_{M_{n2}} \underbrace{+fU_s}_{M_{n3}} \underbrace{+g\left(\cos\alpha\frac{\partial\eta}{\partial y} - \sin\alpha\frac{\partial\eta}{\partial x}\right)}_{M_{n4}} = 0. \tag{A.10}$$

With this transformation M_{s3} and M_{n5} are zero by definition (i.e. bottom friction acts entirely in the streamwise direction, and Coriolis only in the normal direction). To complete the transformation, derivatives in the $x-y$ and $s-n$ coordinate systems are related by the chain rule

$$\frac{\partial}{\partial x} = \frac{\partial}{\partial s}\frac{\partial s}{\partial x} + \frac{\partial}{\partial n}\frac{\partial n}{\partial x} = \cos\alpha\frac{\partial}{\partial s} - \sin\alpha\frac{\partial}{\partial n}, \tag{A.11}$$

$$\frac{\partial}{\partial y} = \frac{\partial}{\partial s}\frac{\partial s}{\partial y} + \frac{\partial}{\partial n}\frac{\partial n}{\partial y} = \sin\alpha\frac{\partial}{\partial s} + \cos\alpha\frac{\partial}{\partial n}, \tag{A.12}$$

where $\partial s/\partial x = \cos\alpha$, $\partial s/\partial y = \sin\alpha$, $\partial n/\partial x = -\sin\alpha$, and $\partial n/\partial y = \cos\alpha$ from Fig. 8. The final relationship needed for the rotation is

$$\frac{\partial\alpha}{\partial s} = \frac{1}{R_s}, \tag{A.13}$$

where $R_s(x, y, t)$ is the streamwise radius of curvature (cf. Kalkwijk and de Vriend, 1980; Gill, 1982), with curvature to the left assumed positive. Expanding the spatial derivatives in Eqs. (A.9) and (A.10) with the chain rule, substituting in the expression for the radius of curvature, and simplifying yields the momentum equations in $s-n$ coordinates

$$\underbrace{\frac{\partial U_s}{\partial t}}_{M_{s1}} \underbrace{+U_s\frac{\partial U_s}{\partial s}}_{M_{s2}} \underbrace{+g\frac{\partial\eta}{\partial s}}_{M_{s4}} \underbrace{+\frac{C_f U_s^2}{H}}_{M_{s5}} = 0, \tag{A.14}$$

$$\underbrace{U_s\frac{\partial\alpha}{\partial t}}_{M_{n1}} \underbrace{+\frac{U_s^2}{R_s}}_{M_{n2}} \underbrace{+fU_s}_{M_{n3}} \underbrace{+g\frac{\partial\eta}{\partial n}}_{M_{n4}} = 0. \tag{A.15}$$

Following the above derivation, the mapping between the $x-y$ and $s-n$ momentum equations is

Local streamwise acceleration:

$$\frac{\partial U_s}{\partial t} = \left(\frac{\partial U}{\partial t}\right)\cos\alpha + \left(\frac{\partial V}{\partial t}\right)\sin\alpha. \tag{A.16}$$

Local rotary acceleration:

$$U_s\frac{\partial\alpha}{\partial t} = \left(\frac{\partial V}{\partial t}\right)\cos\alpha - \left(\frac{\partial U}{\partial t}\right)\sin\alpha. \tag{A.17}$$

Streamwise acceleration:

$$U_s\frac{\partial U_s}{\partial s} = \left(U\frac{\partial U}{\partial x} + V\frac{\partial U}{\partial y}\right)\cos\alpha + \left(U\frac{\partial V}{\partial x} + V\frac{\partial V}{\partial y}\right)\sin\alpha. \tag{A.18}$$

Centrifugal acceleration:

$$\frac{U_s^2}{R_s} = \left(U\frac{\partial V}{\partial x} + V\frac{\partial V}{\partial y}\right)\cos\alpha - \left(U\frac{\partial U}{\partial x} + V\frac{\partial U}{\partial y}\right)\sin\alpha. \quad (A.19)$$

Coriolis acceleration (s-dir):

$$0 = (-fV)\cos\alpha + (fU)\sin\alpha. \quad (A.20)$$

Coriolis acceleration (n-dir):

$$fU_s = (fU)\cos\alpha + (fV)\sin\alpha. \quad (A.21)$$

Pressure gradient (s-dir):

$$g\frac{\partial\eta}{\partial s} = \left(g\frac{\partial\eta}{\partial x}\right)\cos\alpha + \left(g\frac{\partial\eta}{\partial y}\right)\sin\alpha. \quad (A.22)$$

Pressure gradient (n-dir):

$$g\frac{\partial\eta}{\partial n} = \left(g\frac{\partial\eta}{\partial y}\right)\cos\alpha - \left(g\frac{\partial\eta}{\partial x}\right)\sin\alpha. \quad (A.23)$$

Bottom friction (s-dir):

$$\frac{C_f U_s^2}{H} = \left(\frac{C_f\sqrt{U^2+V^2}}{H}U\right)\cos\alpha + \left(\frac{C_f\sqrt{U^2+V^2}}{H}V\right)\sin\alpha. \quad (A.24)$$

Bottom friction (n-dir):

$$0 = \left(\frac{C_f\sqrt{U^2+V^2}}{H}V\right)\cos\alpha - \left(\frac{C_f\sqrt{U^2+V^2}}{H}U\right)\sin\alpha. \quad (A.25)$$

Once values of the $x-y$ momentum terms are known, along with the streamline angle $\alpha(x, y, t)$, the values of the $s-n$ momentum terms can be computed directly. Thus the right-hand sides of Eqs. (A.16)–(A.25) are calculated and the left-hand sides of Eqs. (A.16)–(A.25) are the physical quantities to interpret. This methodology is useful because we retain the computational ease of working in a standard $x-y$ coordinate system, and with a simple transform we gain the interpretational advantages of the $s-n$ coordinate system. In a fully nonlinear system with strongly curving flow, this can be a valuable aid in understanding the dynamics.

References

Awaji, T., Imasato, N., Kunishi, H., 1980. Tidal exchange through a strait: a numerical experiment using a simple model basin. Journal of Physical Oceanography 10, 1499–1508.

Black, K., Hatton, D., Rosenberg, M., 1993. Locally and externally driven dynamics of a large semi-enclosed bay in Southern Australia. Journal of Coastal Research 9 (2), 509–538.

Brown, C.A., Jackson, G.A., Brooks, D.A., 2000. Particle transport through a narrow tidal inlet due to tidal forcing and implications for larval transport. Journal of Geophysical Research 105 (C10), 24141–24156.

Chadwick, D.B., Largier, J.L., 1999. Tidal exchange at the bay-ocean boundary. Journal of Geophysical Research 104 (C12), 29901–29924.

David, L.T., Kjerfve, B., 1998. Tides and currents in a two-inlet coastal lagoon: Laguna de Terminos, Mexico. Continental Shelf Research 18, 1057–1079.

Doyle, B.E., Wilson, R.E., 1978. Lateral dynamic balance in the Sandy Hook to Rockaway Point transect. Estuarine Coastal and Marine Science 6, 165–174.

Dyer, K.R., 1997. Estuaries, A Physical Introduction, 2nd Edition. Wiley, Chichester.

Garvine, R.W., 1987. Estuary plumes and fronts in shelf waters: a layer model. Journal of Physical Oceanography 17 (11), 1877–1896.

Garvine, R.W., 1995. A dynamical system for classifying buoyant coastal discharges. Continental Shelf Research 15 (13), 1585–1596.

Gill, A.E., 1982. Atmosphere-Ocean Dynamics. Academic Press, San Diego.

Hansen, D.V., Rattray, M., 1966. New dimensions in estuary classification. Limnology and Oceanography 11 (3), 319–326.

Hayes, M.O., 1979. Barrier island morphology as a function of tidal and wave regime. In: Leatherman, S.P. (Ed.), Barrier Islands from the Gulf of St. Lawrence to the Gulf of Mexico. Academic Press, New York, pp. 1–27.

Hearn, C.J., Hunter, J.R., Imberger, J., van Senden, D., 1985. Tidally induced jet in Koombana Bay, Western Australia. Australian Journal of Marine and Freshwater Research 36, 453–479.

Hench, J.L., Luettich Jr., R.A., in review. Transient tidal circulation and momentum balances at a shallow inlet. Journal of Physical Oceanography, submitted for publication.

Imasato, N., 1983. What is tide-induced residual current? Journal of Physical Oceanography 13, 1307–1317.

Imasato, N., Fujio, S., Zhang, Q., Awaji, T., Akitomo, K., 1994. Three-dimensional numerical experiments on tidal exchange through a narrow strait in a homogeneous and a stratified sea. Journal of Oceanography 50, 119–139.

Jay, D.A., Smith, J.D., 1988. Residual circulation in and classification of shallow estuaries. In: Dronkers, J., van

Leussen, W. (Eds.), Physical Processes in Estuaries. Springer, Heidelberg, pp. 19–41.

Jay, D.A., Geyer, W.R., Montgomery, D.R., 2000. An ecological perspective on estuarine classification. In: Hobbie, J.E. (Ed.), Estuarine Science, A Synthetic Approach to Research and Practice. Island Press, New York, pp. 149–176.

Kalkwijk, J.P.T., de Vriend, H.J., 1980. Computation of flow in shallow river bends. Journal of Hydraulic Research 18 (4), 327–342.

Kapolnai, A., Werner, F.E., Blanton, J.O., 1996. Circulation, mixing, and exchange processes in the vicinity of tidal inlets: a numerical study. Journal of Geophysical Research 101 (C6), 14253–14268.

Kourafalou, V.H., Oey, L.-Y., Wang, J.D., Lee, T.N., 1996. The fate of river discharge on the continental shelf 1. Modeling the river plume and inner shelf coastal current. Journal of Geophysical Research 101 (C2), 3415–3434.

Liu, J.T., 1992. The influence of episodic weather events on tidal residual currents: a case study at Sebastian Inlet. Estuaries 15 (2), 109–121.

Luettich Jr., R.A., Westerink, J.J., Scheffner, N.W., 1992. ADCIRC: an advanced three-dimensional model for shelves, coasts, and estuaries, Report 1: Theory and methodology of ADCIRC 2DDI and ADCIRC 3-DL. Dredging Research Program Technical Report DRP-92-6, Coastal Engineering Research Center, US Army Corps of Engineers, Waterways Experiment Station, Vicksburg, MS, 141pp.

Luettich Jr., R.A., Hench, J.L., Fulcher, C.W., Werner, F.E., Blanton, B.O., Churchill, J.H., 1999. Barotropic tidal and wind driven larvae transport in the vicinity of a barrier island inlet. Fisheries Oceanography 8 (Suppl. 2), 190–209.

Mariano, C.G., FitzGerald, D.M., 1991. Wave-current interaction at Wells Inlet, Maine. In: Kraus, N.C., Gingerich, K.J., Kriebel, D.L. (Eds.), Proceedings of Coastal Sediments '91. American Society of Civil Engineers, New York, pp. 1356–1374.

Militello, A., Zarillo, G.A., 2000. Tidal motion in a complex inlet and bay system, Ponce de Leon Inlet, Florida. Journal of Coastal Research 16 (3), 840–852.

Militello, A., Kraus, N.C., Brown, M.E., 2000. Regional coastal and inlet circulation modeling with application to Long Island, New York. In: Proceedings 13th Annual National Conference on Beach Preservation Technology. Florida Shore & Beach Preservation Association, Tallahassee, FL, pp. 191–201.

Ridderinkhof, H., 1988. Tidal and residual flows in the Western Dutch Wadden Sea I: numerical model results. Netherlands Journal of Sea Research 22, 1–21.

Signell, R.P., Geyer, W.R., 1991. Transient eddy formation around headlands. Journal of Geophysical Research 96 (C2), 2561–2575.

Smith, J.B., FitzGerald, D.M., 1994. Sediment transport patterns at the Essex River Inlet ebb-tidal delta, Massachusetts, USA. Journal of Coastal Research 10 (3), 752–774.

Stommel, H., Farmer, H.G., 1952. On the nature of estuarine circulation, Part III, Chapter 7, Classification of estuaries by salinity structure. Woods Hole Oceanographic Institution Technical Report Ref. No. 52–88, 131pp.

Wheless, G.H., Valle-Levinson, A., 1996. A modeling study of tidally driven estuarine exchange through a narrow inlet onto a sloping shelf. Journal of Geophysical Research 101 (C11), 25675–25687.

Wolanski, E., Drew, E., Abel, K.M., O'Brien, J., 1988. Tidal jets, nutrient upwelling and their influence on the productivity of the alga *Halimeda* in the Ribbon Reefs, Great Barrier Reef. Estuarine Coastal and Shelf Science 26, 169–201.

Wong, K.-C., DiLorenzo, J., 1988. The response of Delaware's inland bays to ocean forcing. Journal of Geophysical Research 93 (C10), 12525–12535.